Preliminary estimate of the impact of support structures on the aerodynamic performance of very large wind farms

Preliminary estimate of the impact of support structures on the aerodynamic performance of very large wind farms

Lun Ma*, Takafumi Nishino

Cranfield University, Cranfield, Bedfordshire MK43 0AL, United Kingdom

*E-mail: l.ma@cranfield.ac.uk

Abstract. An extended theoretical model, which is based on a two-scale coupled momentum conservation argument, is proposed to estimate aerodynamic effects of support structures on the performance of ideal very large wind farms. A key implication of this extended model is that the parameter $(A_S/A)\cdot C_D^*$, where A and A_S are the rotor swept area and support-structure frontal projected area, respectively, and C_D^* is an effective support-structure drag coefficient, plays an important role in the design of very large wind farms. In particular, the optimal farm density tends to decrease as the normalised support-structure drag increases. To validate this extended model, Wall-Modelled Large-Eddy Simulations (WMLES) of a periodic array of actuator discs with and without support structures are conducted; results agree qualitatively with the model.

1. Introduction

Despite a number of studies reported on the modelling of wind turbine wakes, the effects of support structures on wind farm performance have been relatively less investigated to date. For instance, the original 'top-down' model of Frandsen [1] and the later improvements of Calaf et al. [2] and Meneveau [3] have not included the impact of support structures explicitly. In this paper, an extension to the two-scale momentum model of Nishino [4] (see also Nishino and Hunter [5]) is presented. This extended model now takes into account the aerodynamic impact of turbine support structures (towers). In addition, a series of CFD simulations are conducted to validate this extended theoretical model.

2. Theory

The original two-scale coupled momentum model [4, 5] has been designed to predict the performance of idealised very large wind farms. The atmospheric boundary layer (ABL) is assumed to be driven by a constant pressure gradient, as with Calaf et al. [2]. A momentum balance equation can then be derived by considering two different ABL's: one is the 'undisturbed' or 'natural' ABL before farm construction, and the other is the 'disturbed' ABL after farm construction. The new modification in the present study is to add the drag force due to turbine support structures in the momentum balance equation as follows:

$$\langle\tau_w\rangle S + T + D = \tau_{w0} S \tag{1}$$

where $\langle\tau_w\rangle$ is the bottom shear stress (wind-induced shear stress on the land or sea surface, depending on whether the farm is onshore or offshore) averaged across the area S, which is the average land/sea surface area per each turbine, T is the thrust on one rotor, D is the drag due to its support structure (tower) and τ_{w0} is the 'natural' bottom shear stress, i.e. shear stress on the land/sea surface at the construction site before constructing the wind farm. The thrust T and drag D are then represented using 'local' thrust and drag coefficients C_T^* and C_D^* (i.e. based on a locally-averaged wind speed) as

$$T = \frac{1}{2}\rho U_F^2 A \cdot C_T^* \tag{2}$$

$$D = \frac{1}{2}\rho U_F^2 A_s \cdot C_D^* \tag{3}$$

where ρ is air density, A and A_S are the turbine swept area and support-structure frontal projected area, respectively, and U_F is the average wind speed across the wind farm layer defined in [4]. This layer is typically two to three times as high as the turbine hub height; see [4] and [5] for further details.

Following the original two-scale momentum model [4], C_T^* is modelled using the classical actuator disc theory; this is a strong simplification but tends to result in a reasonably good agreement with 3D RANS simulations [6] and Large-Eddy Simulations [7]. Eventually, Eq. (1) can be transformed into

$$1 - \beta^\gamma = \frac{\Lambda}{C_{f0}} \cdot \beta^2 \cdot \left(4\alpha(1-\alpha) + \frac{A_S}{A} C_D^*\right) \tag{4}$$

where $\alpha = U_T/U_F$ (U_T is the average wind speed across A), $\beta = U_F/U_{F0}$ (U_{F0} is the farm-layer wind speed observed before farm construction), $\Lambda = A/S$ is the farm density, $C_{f0} = \tau_{w0}/\frac{1}{2}\rho U_{F0}^2$ is a natural friction coefficient and $\gamma = \log_\beta(\langle\tau_w\rangle/\tau_{w0})$ is an empirical parameter to model the wall shear stress ratio $\langle\tau_w\rangle/\tau_{w0}$ [4]. The value of γ is typically between 1.5 and 2, but in the present study we assume γ = 2 for simplicity. Since Eq. (4) can be solved to obtain β as a function of α (for a given set of model inputs: γ, Λ/C_{f0} and $(A_s/A)C_D^*$), we can calculate the power coefficient (C_P) of a turbine in the farm:

$$C_P = \frac{\text{Power}}{\frac{1}{2}\rho U_{F0}^3 A} = \frac{TU_T}{\frac{1}{2}\rho U_{F0}^3 A} = \frac{U_F^2 U_T}{U_{F0}^3} \cdot 4\alpha(1-\alpha) = \beta^3 \cdot 4\alpha^2(1-\alpha) \tag{5}$$

In addition, the normalised power density η is defined to represent the performance of the entire farm:

$$\eta = \frac{\text{Power}}{\tau_{w0} U_{F0} S} = \frac{\frac{1}{2}\rho U_{F0}^3 A \cdot C_P}{\tau_{w0} U_{F0} S} = \Lambda \cdot \frac{1}{C_{f0}} \cdot C_P \tag{6}$$

Some example solutions are presented here to show graphically the relationships between the key parameters in the theoretical model, as well as how the influence of support structures on the optimal farm density may be estimated from the model. Traditional turbine spacing for offshore wind farms is around 7*d*, where *d* is the rotor diameter, and could potentially be as large as 15*d* [8]. Furthermore, for an average wind speed of 10m/s, the 'natural' friction coefficient of the sea surface can be assumed to be around 0.002 (depending on various wind-wave interaction parameters) [9]. Therefore, a typical range for the effective farm density (Λ/C_{f0}) of offshore wind farms could be around 2 to 8. In this study we consider a wider range of 0 to 10.

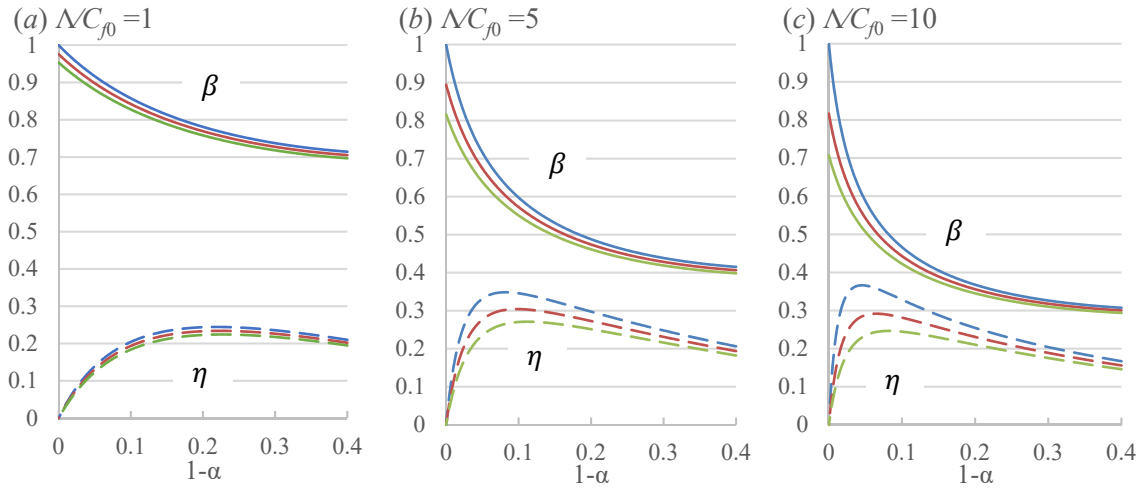

Figure 1. Effects of support-structure drag on the performance of very large wind farms: solid and dashed lines show β and η, respectively, and $(1-\alpha)$ is the local axial induction factor of each rotor. Blue: $(A_s/A)C_D^* = 0$; red: $(A_s/A)C_D^* = 0.05$; and green: $(A_s/A)C_D^* = 0.1$.

According to the most common monopile-type foundation design for offshore wind turbines and the drag coefficient range for a circular cylinder under relevant Reynolds number conditions [10] [11], the value of the normalised support-structure drag ($(A_s/A)C_D^*$) is expected to be up to about 0.1 in most cases. Figure 1 shows the variations of β and η against the 'local' axial induction factor $(1-\alpha)$, for three ideal wind farms with Λ/C_{f0} values of 1, 5 and 10, respectively, with three $(A_s/A)C_D^*$ values of 0, 0.05 and 0.1. The overall wind farm performance is hardly influenced by the support structures when the effective farm density is small ($\Lambda/C_{f0} = 1$). However, as the farm density increases, the support-structure effect becomes more obvious; for example, at $\Lambda/C_{f0} = 5$, the maximum power density for $(A_s/A)C_D^* = 0.1$ ($\eta_{max} \approx 0.27$ at $\alpha \approx 0.89$) is more than 20% lower than that for $(A_s/A)C_D^* = 0$, i.e. for the case without support structures ($\eta_{max} \approx 0.35$ at $\alpha \approx 0.92$).

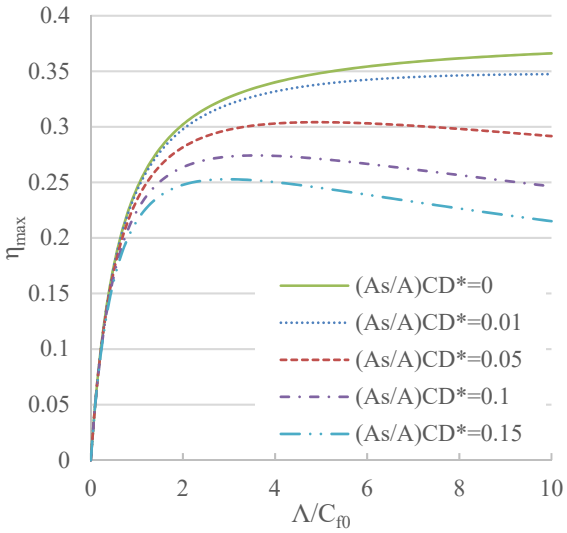

Figure 2. The maximum normalised power density η_{max} against the effective farm density Λ/C_{f0} for various normalised support-structure drag $(A_s/A)C_D^*$.

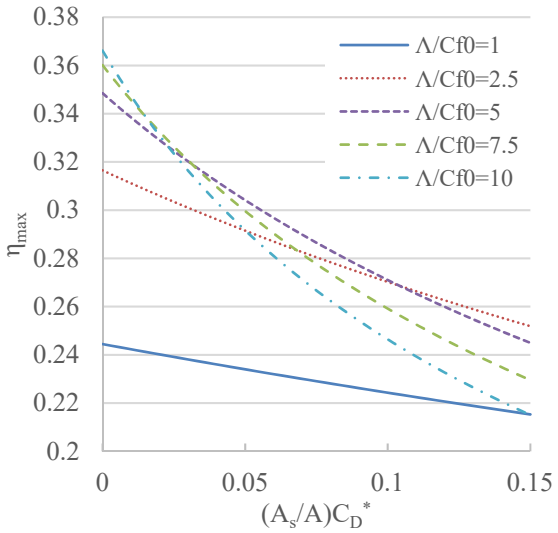

Figure 3. The maximum normalised power density η_{max} against the normalised support-structure drag $(A_s/A)C_D^*$ for various effective farm density Λ/C_{f0}.

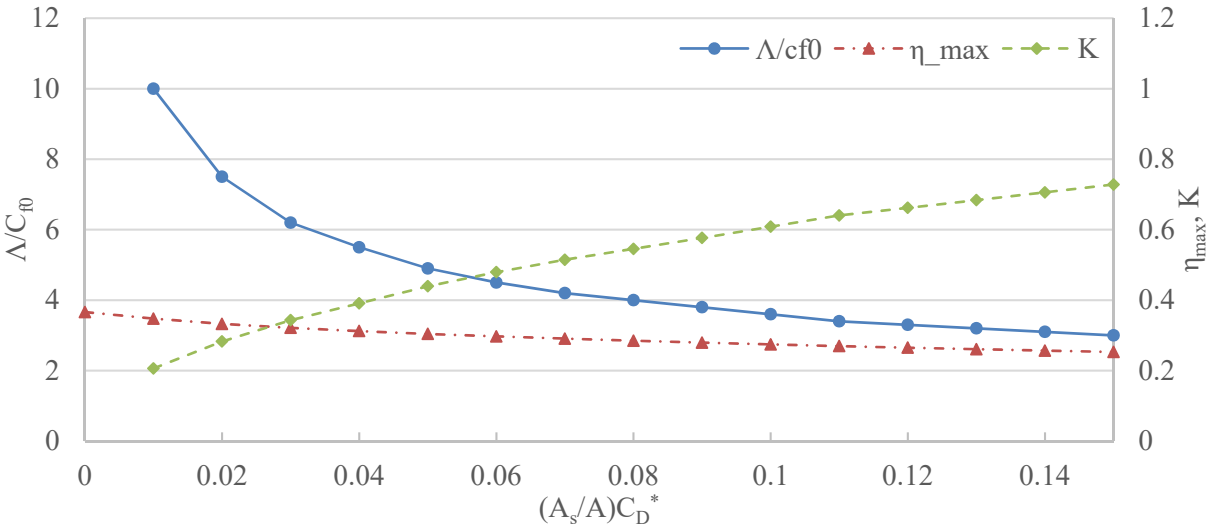

Figure 4. The optimal values of effective farm density Λ/C_{f0}, rotor resistance $K(=\frac{4(1-\alpha)}{\alpha})$ and the maximum normalised power density η_{max} (for ideal very large wind farms) plotted against the normalised support-structure drag $(A_s/A)C_D^*$.

Figures 2 and 3 summarise the effects of farm density and support-structure drag on the maximum farm performance. When the support-structure drag is zero, this model goes back to the original two-scale coupled momentum model [4], in which the maximum power density η_{max} always increases with the effective farm density Λ/C_{f0}. However, when the support-structure effect is considered, the power density increases with the farm density only up to an optimal value, above which the power will decrease (Figure 2). Importantly, the impact of support-structure drag on the maximum power density becomes more and more significant as the farm density increases (Figure 3). This is basically because the optimal rotor thrust decreases [6] and therefore the relative importance of support-structure drag increases as the farm density increases. It should be noted that, whilst the rotor thrust can be reduced or optimised by changing the rotor operating conditions, the support-structure drag cannot be reduced unless the design of support structures is changed. This suggests that the farm density of a very large wind farm should be optimised by taking into account the design of support structures.

Figure 4 shows how the optimal values of the effective farm density (Λ/C_{f0}) and rotor resistance ($K = T/\frac{1}{2}\rho U_T^2 A = 4(1-\alpha)/\alpha$) change with the normalised support-structure drag ($(A_s/A)C_D^*$). Also plotted are the maximum normalised power density (η_{max}) values obtained from such an optimisation.

3. CFD Simulations

Due to the wide range of design parameters involved, the theoretical results presented above cannot be entirely verified using CFD simulations; hence only a few example cases are simulated focusing on the impact of support structures. The CFD model employed is a Wall-Modelled Large-Eddy Simulation (WMLES) of a pressure-driven ABL coupled with localised streamwise momentum sinks representing turbine rotors and support structures. The simulations are performed for infinitely-large (periodic) staggered arrays of turbines with and without support structures.

3.1. Computational domain and flow conditions

Unlike the previous validation studies of the two-scale momentum model [4, 6] that used Reynolds-averaged Navier-Stokes (RANS) simulations of a single turbine in a small periodic domain, we consider four turbines in a larger periodic domain as shown in Figure 5. The turbine spacing is $L_x \times L_y = 7d \times 7d$ (with a lateral displacement of $\Delta_y = 3.5d$ for the staggered arrangement) and the height of the domain (L_z) is $10d$ with a clearance of $0.5d$ between the ground and rotors; therefore, the size of the computational domain is $2L_x \times 2L_y \times L_z = 14d \times 14d \times 10d$. The origin of the coordinates is at the centre of the horizontal plane at the turbine hub height. The rotor diameter d is 100m. This configuration is identical to one of the cases employed in the previous RANS study by Zapata et al. [6], except that four turbines are simulated (instead of one) in the present WMLES study.

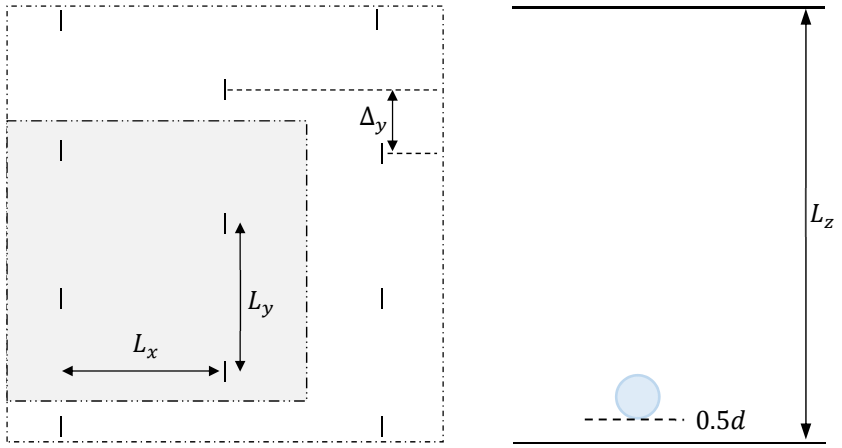

Figure 5. Schematic of turbine arrangements. Left: horizontal plane (computational domain in grey); right: rotor position in the vertical direction.

Periodic boundary conditions are applied to both streamwise and lateral directions, whereas the top of the domain is treated as a symmetry boundary. In addition, the bottom of the domain is treated as a rough wall boundary; more details will be explained in the next subsection. As with the previous study by Zapata et al. [6], the air flow is driven by a constant pressure gradient. This pressure gradient value is calculated from an 'empty box' simulation, in which a constant mass flow rate (corresponding to a vertically-averaged wind speed of 10m/s for the entire domain) is given as the driving force to obtain the pressure gradient for a fully developed boundary layer flow without any turbines.

3.2. Computational methods

All calculations are carried out using the commercial CFD solver 'ANSYS FLUENT 17.2' [12]. The original version of the Detached-Eddy Simulations (DES) approach using the Spalart-Allmaras model (often referred to as DES97) is employed as a mean to conduct simple WMLES [13, 14], i.e. the flow in the vicinity of the bottom boundary is treated as RANS and the rest of the domain is treated as LES. The reason for employing DES97, instead of more advanced DES approaches, is that the thickness of the RANS layer can be fixed and controlled explicitly by adjusting near-wall mesh resolutions. As will be described later, we employ a uniform horizontal mesh resolution of 10m near the bottom boundary for the entire domain, meaning that the thickness of the RANS layer is 6.5m in this study (as the DES model coefficient $C_{DES} = 0.65$ in DES97). In addition, similarly to the previous RANS study [6], the effect of bottom roughness is modelled using a modified wall function for 'fully rough' walls available in FLUENT [12]. The two roughness parameters, namely the nominal 'sand-grain' type roughness height k_s and the roughness constant C_s, are set to be 1m and 0.5, respectively (this corresponds to an aerodynamic roughness length of $z_0 = 0.051\text{m}$ since $k_s = (E/C_s)z_0$ [15], where $E = 9.793$ is an empirical value employed in FLUENT [12]). The density and viscosity of the working fluid (air) are constant in this study: $\rho = 1.225\text{kg/m}^3$ and $\mu = 1.789 \times 10^{-5}\text{kg/m-s}$, respectively.

The effects of turbine rotors and support structures are both modelled as streamwise momentum losses, i.e. both rotors and support structures are modelled as stationary permeable surfaces of zero thickness with a momentum loss factor (K for the rotors and K_s for the support structures), by which their resistance can be changed. Specifically, the (instantaneous) momentum loss is calculated as

$$M_x = K_{(s)} \cdot \frac{1}{2}\rho u^2 \tag{7}$$

where u is the (instantaneous) streamwise velocity. Since the time-averaged rotor thrust and support-structure drag can be obtained as $T = \overline{\int M_x \, \mathrm{d}A}$ and $D = \overline{\int M_x \, \mathrm{d}A_s}$, we may calculate the 'local' rotor thrust coefficient C_T^* and 'local' support-structure drag coefficient C_D^* as

$$C_T^* = \frac{T}{\frac{1}{2}\rho U_F^2 A} = K\frac{\overline{\int u^2 \mathrm{d}A}}{U_F^2 A} \tag{8}$$

$$C_D^* = \frac{D}{\frac{1}{2}\rho U_F^2 A_s} = K_s\frac{\overline{\int u^2 \mathrm{d}A_s}}{U_F^2 A_s} \tag{9}$$

However, for the purpose of comparison with the theoretical model, which is essentially for the time-averaged flow field and does not consider any velocity fluctuations in time, here we calculate C_T^* and C_D^* directly from the time-averaged flow field as

$$C_T^* = K\frac{U_T^2}{U_F^2} \tag{10}$$

$$C_D^* = K_s\frac{U_S^2}{U_F^2} \tag{11}$$

where U_T and U_S are the spatial- and time-averaged streamwise velocity over the rotor area A and the support-structure area A_s, respectively. Note that the values of C_T^* and C_D^* calculated from Eqs (10) and (11) are a little different from those from Eqs (8) and (9) since in general $\overline{u^2} > \bar{u}^2$ but we ignore this small difference in this study. Similarly, since the time-averaged rotor power can be obtained as $P = \overline{\int M_x u \, \mathrm{d}A}$, the rotor power coefficient C_P may be calculated as

$$C_P = \frac{P}{\frac{1}{2}\rho U_{F0}^3 A} = K\frac{\overline{\int u^3 \mathrm{d}A}}{U_{F0}^3 A} \tag{12}$$

but again, for the purpose of comparison with the theoretical model, here we calculate C_P as

$$C_P = K\frac{U_T^3}{U_{F0}^3} = K\alpha^3\beta^3 \tag{13}$$

In order to simulate the support-structure drag in a simplified manner, we consider that the support structure is located only below each rotor disc (as shown later in Figure 7). The areas of the rotor disc and support structure are fixed for all cases in this study (with a ratio of A_s/A = 0.119), which means only the value of K_s needs to be modified to vary the support-structure drag. Here we consider five different K_s values: 0, 0.542, 1.716, 3 and 4. The two intermediate values (0.542 and 1.716) were selected based on our initial speculation that these two values would result in C_D^* = 0.42 and 0.84 (and hence $(A_s/A)C_D^*$ = 0.05 and 0.1) if a theoretical relationship $C_D^* = K_s\left(\frac{4}{4+K_s}\right)^2$ (following the actuator disc theory) was satisfied; however, we eventually found that the actual C_D^* values obtained from the simulations were smaller, as summarised in Table 1. This difference could be due to the rather coarse mesh used for the tower as well as the flow interactions with the surroundings (ground and rotor disc).

Table 1 Summary of support structure characteristics

Case	K_s	$C_{D(initial\ guess)}^*$	$C_{D(CFD)}^*$	$(A_s/A)C_D^*$
1	0	0	0	0
2	0.542	0.42	0.270	0.0321
3	1.716	0.84	0.577	0.0687
4	3	0.98	0.642	0.0765
5	4	1	0.743	0.0884

The numerical methods employed are nominally second-order accurate in space and time, using a bounded central difference scheme for spatial discretisation of the momentum equations and a second-order implicit scheme for temporal discretisation. The SIMPLE algorithm is used for pressure-velocity coupling. A constant time step size of 0.1s is adopted with 10 iterations at each time step. Each farm simulation has been run for 300,000 time steps initially, followed by another 50,000 time steps to obtain the time-averaged results. Figure 6 shows an example of the time history of the streamwise velocity averaged over the four discs, showing that the simulation has been run long enough to obtain reliable time-averaged results.

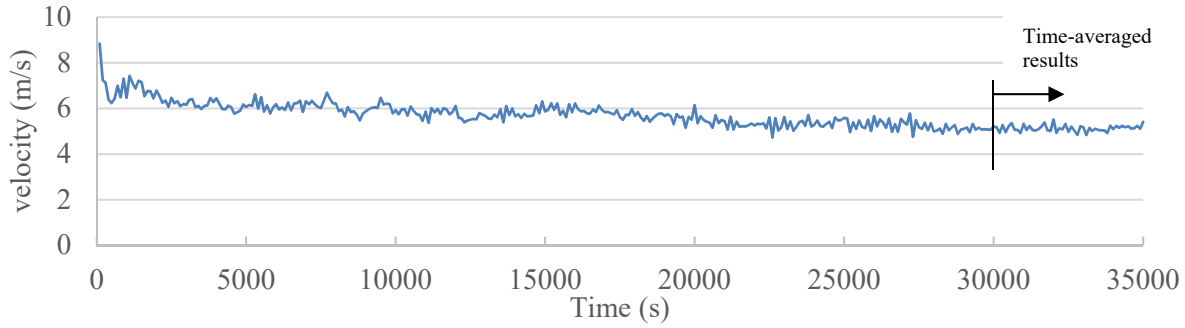

Figure 6. Time history of the streamwise velocity averaged over four discs in Case 3 (sampling rate is every 100s).

3.3. Computational mesh

Multi-block structured meshes are created in this study. A 2D mesh for a y-z plane is generated first and then extruded to streamwise direction (x) to form the 3D mesh with hexahedral cells. An 'O-grid' mesh topology is used inside and around the rotor disc, to distribute cells along the edge of the disc (Figure 7).

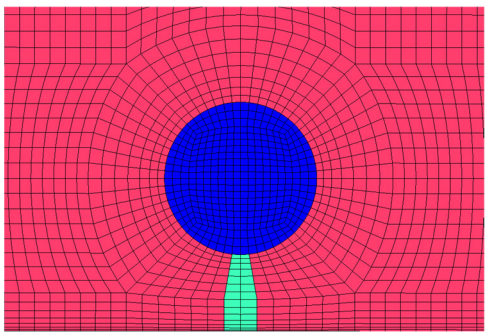

Figure 7. Cross-sectional mesh for the rotor disc (blue), tower (light green) and surrounding area.

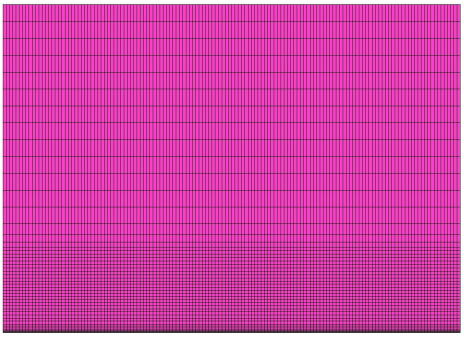

Figure 8. Mesh on a lateral plane (at $y = 0$) for the entire computational domain.

The smallest mesh spacing is 1m, which is for the first cells above the bottom surface in the vertical (z) direction. For the horizontal (x and y) directions, however, a constant spacing of 10m is employed for the entire domain (Figure 8). The total number of cells is 1.3×10^6.

3.4. Results and discussion

Table 2 compares results of 'empty box' simulations using WMLES and RANS. For RANS, we have tested the *k-ω* SST model as well as the Spalart-Allmaras model for comparison. Also presented for comparison are results from the previous RANS study by Zapata et al. [6] using the Standard *k-ε* model. The (spatial- and time-averaged) natural bottom shear stress τ_{w0} obtained from WMLES is about 14% smaller than the Spalart-Allmaras RANS result. Note that this trend, that WMLES using DES97 tends to yield a smaller wall shear stress value, is in agreement with [13]. It should also be noted that the quantitative accuracy of the prediction of τ_{w0} for a given roughness height is, in principle, not our primary concern, because the theoretical results to be compared with these CFD results for validation (such as the power coefficient C_P) are given as a function of Λ/C_{f0} (not as a function of the roughness height). However, the value of Λ/C_{f0} obtained from the current WMLES is about 26% larger than the Spalart-Allmaras RANS result (this is because of not only the difference in τ_{w0} but also the difference in U_{F0}) and such a large over-prediction of Λ/C_{f0} may not be desirable (as will be discussed later).

Table 2 Comparison of 'empty box' results between WMLES and RANS

	τ_{w0} (Pa)	Pressure gradient (Pa/m)	U_{F0} (m/s)	H_F/d	Λ/C_{f0}
WMLES	0.1785	-1.785×10^{-4}	8.89	2.8	4.35
Spalart-Allmaras (RANS)	0.2081	-2.081×10^{-4}	8.55	2.6	3.45
k-ω SST (RANS)	0.2364	-2.364×10^{-4}	8.59	2.6	3.06
Standard *k-ε* (RANS) [6]	0.2597	-2.597×10^{-4}	8.34	2.6	2.63

Key results from the farm simulations (using WMLES) are summarised in Table 3, where C_P is calculated using Eq. (13). It can be seen that the turbine support structures have a minor effect on the value of γ, which is slightly higher than that obtained in the previous RANS study [6] but still lower than $\gamma = 2$ proposed as a theoretical upper limit in the two-scale momentum model [4].

Table 3 Summary of farm simulation results ($H_F = 280$m, $U_{F0} = 8.89$m/s)

Case	K	U_F (m/s)	U_T (m/s)	α	β	τ_w/τ_{w0}	γ	C_P
1	0.5	5.94	5.16	0.869	0.668	0.498	1.73	0.0977
2	0.5	5.84	5.16	0.884	0.657	0.483	1.73	0.0979
3	0.5	5.74	5.13	0.893	0.645	0.473	1.71	0.0957
4	0.5	5.56	4.80	0.863	0.625	0.425	1.82	0.0786
5	0.5	5.31	4.69	0.883	0.597	0.407	1.74	0.0733

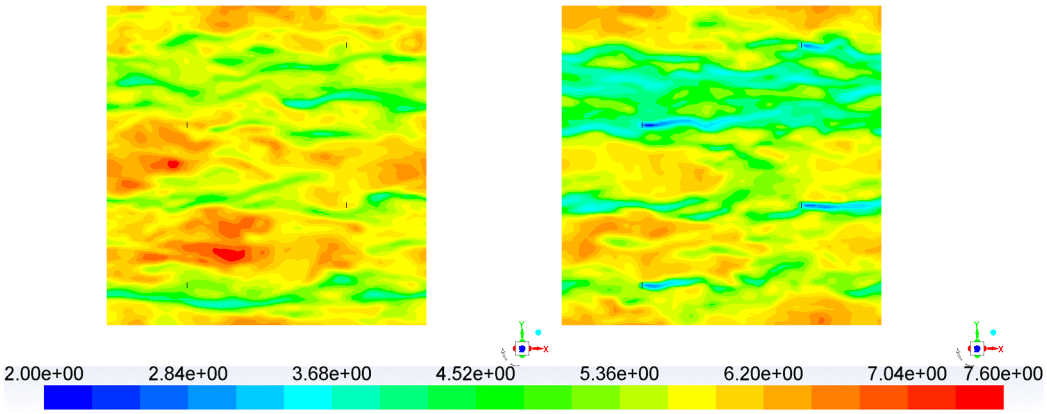

Figure 9. Contours of instantaneous streamwise velocity [m/s] at the tower mid-height. Left: Case 1 (no towers, $K_s = 0$), right: Case 5 (with towers, $K_s = 4$).

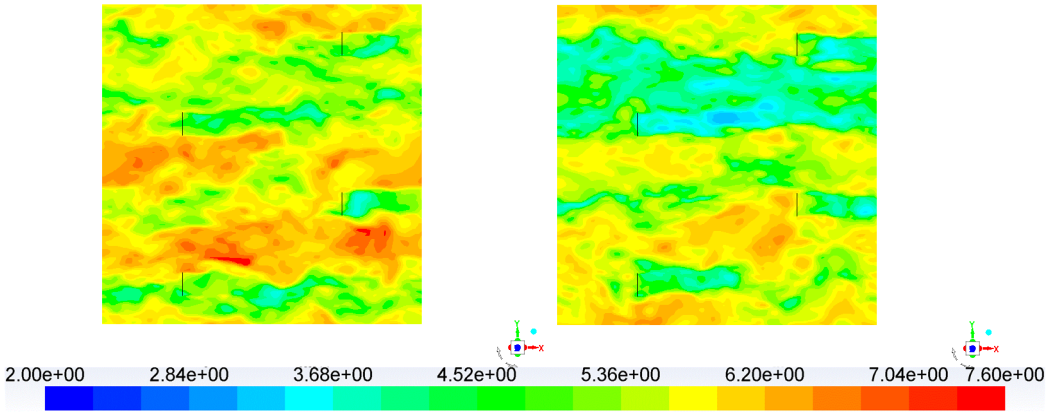

Figure 10. Contours of instantaneous streamwise velocity [m/s] at the rotor hub-height. Left: Case 1 (no towers, $K_s = 0$), right: Case 5 (with towers, $K_s = 4$).

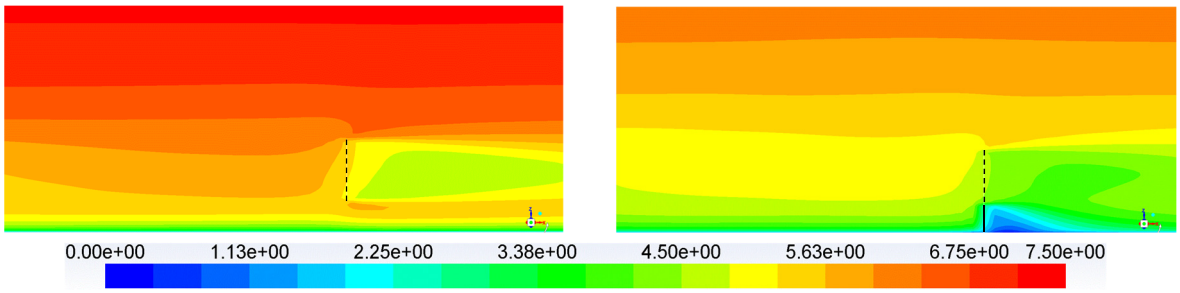

Figure 11. Contours of time-averaged streamwise velocity [m/s] on a lateral plane across the centre of a turbine; dashed and solid lines show the rotor and tower positions, respectively. Left: Case 1 (no towers, $K_s = 0$), right: Case 5 (with towers, $K_s = 4$).

Before comparing the main results (such as C_P) with the theoretical model, we briefly discuss key differences in the flow field between Case 1 (no towers) and Case 5 (with highest-resistance towers). Figures 9 and 10 show contour plots of instantaneous streamwise velocity on a horizontal plane at the tower mid-height and at the rotor hub-height, respectively, showing turbine wakes generated in the two cases. In particular, a narrow but clear wake pattern is visible behind each tower (Figure 9-right), even though the towers have been modelled in a rather simplified manner. In addition, not only at the tower mid-height but also at the rotor hub-height, it can be seen that the streamwise velocity is (on average) slowed down due to the high support-structure drag. This can be seen more clearly in Figure 11, which

shows contours of time-averaged streamwise velocity on a lateral plane at the centre of a turbine. This figure also suggests that the tower tends to cause an effect similar to the local blockage effect [16], i.e. the acceleration of flow below the rotor (that happens if there is no tower, Figure 11-left) is prevented by the tower (Figure 11-right); such a blockage effect is not accounted for in the theoretical model.

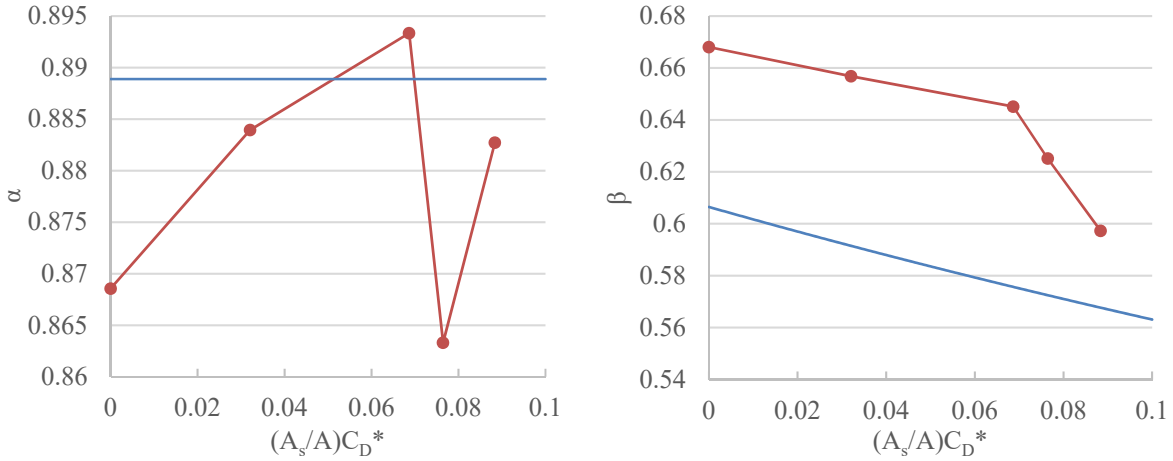

Figure 12. Comparison of α (left) and β (right) between CFD (red) and theoretical model (blue).

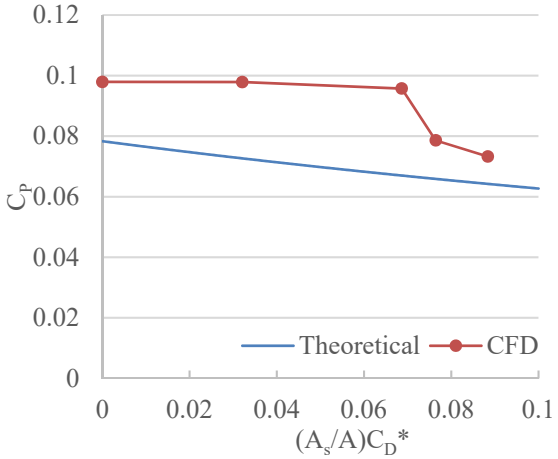

Figure 13. Comparison of C_P between CFD (red) and theoretical model (blue).

Now we compare the values of α, β and C_P obtained from the farm simulations with the theoretical model predictions. In the theoretical model, α is constant at 8/9 when the rotor resistance K is fixed at 0.5 (because $K = 4(1-\alpha)/\alpha$); however, this is not the case in the CFD simulations, where α varies slightly with the support-structure drag (Figure 12-left); this could be mainly due to the blockage effect caused by the towers. On the other hand, both CFD and theoretical model predict that β decreases as the support-structure drag increases, although the β values are about 5 to 12% higher in CFD than in the theoretical model (Figure 12-right). This discrepancy in β is much larger than that found in the previous RANS study [6] (where the discrepancy was less than 3% for the case without towers, compared to 10% in this study) and the reason for this is not very clear at this stage. A possible explanation is that the present WMLES yielded a much larger Λ/C_{f0} value compared to RANS (as shown earlier in Table 2) and hence the theoretical model predicted much lower β values in this study than in the previous study [6]. (This suggests that uncertainties in the calculation of C_{f0} in the 'empty box' simulation need to be assessed carefully in a future study, e.g. how the computational domain size affects C_{f0}.) Eventually, the values of C_P obtained from the present simulations are higher than the theoretical predictions (Figure 13) mainly due to the large discrepancy in β (since $C_P = K\alpha^3\beta^3$ as shown in Eq. (13)), although the trend is similar, i.e. C_P tends to decrease as the support-structure drag increases.

4. Conclusions

An extended two-scale coupled momentum model has been proposed in this study to estimate potential impacts of support-structure drag on the aerodynamic performance of a very large wind farm. A key implication of this extended theoretical model is that the support structures may have an increasingly important influence on the overall farm performance as the farm density (or the number of turbines installed in a given farm area) increases. This is essentially because the optimal rotor thrust decreases and therefore the relative importance of support-structure drag increases as the farm density increases. This also means that the optimal farm density should depend on the level of support-structure drag, or more specifically, the normalised support-structure drag $(A_s/A)C_D^*$ defined in this study.

A series of CFD simulations (WMLES) of a periodic staggered array of wind turbines (with both rotors and support structures modelled simply as streamwise momentum losses) has also been carried out for comparison with the theoretical model. Five different resistance (K_s) values were employed for the support structures (towers) with all other conditions unchanged. The results show that the average wind speed through the nominal farm layer tends to decrease, and so does the rotor power, as the level of support-structure drag increases; this agrees qualitatively with the theoretical model. However, the quantitative agreement was not as great as that found in the previous RANS study (for the case without support structures) [6]. Further investigations are required to understand the cause of this discrepancy.

References

[1] S. Frandsen, 1992, "On the wind speed reduction in the center of large clusters of wind turbines," *J. Wind Eng. Ind. Aerodyn.* Vol. 39, 251-265.
[2] M. Calaf, C. Meneveau and J. Meyers, 2010, "Large eddy simulation study of fully developed wind-turbine array boundary layers," *Physics of Fluids*, vol. 22, no. 1, 015110.
[3] C. Meneveau, 2012, "The top-down model of wind farm boundary layers and its applications," *Journal of Turbulence*, vol. 13, no. 7, 1-12.
[4] T. Nishino, 2016, "Two-scale momentum theory for very large wind farms," *Journal of Physics: Conference Series*, vol. 753, 032054.
[5] T. Nishino and W. Hunter, "Tuning turbine rotor design for very large wind farms," (under review; preprint available at https://arxiv.org/pdf/1803.03984).
[6] A. Zapata, T. Nishino and P.-L. Delafin, 2017, "Theoretically optimal turbine resistance in very large wind farms," *Journal of Physics: Conference Series*, vol. 854, 012051.
[7] N.S. Ghaisas, A.S. Ghate, S.K. Lele, 2017, "Farm efficiency of large wind farms: evaluation using large eddy simulation," *Proc. 10th International Symposium on Turbulence and Shear Flow Phenomena*, Chicago, USA. http://tsfp10.org/TSFP10_program/2/380.pdf.
[8] J. Meyers and C. Meneveau, 2012, "Optimal turbine spacing in fully developed wind farm boundary layers", *Wind Energy*, vol. 15, no. 2, 305-317
[9] W. Drennan, P. Taylor, M. Yelland, 2005, "Parameterizing the Sea Surface Roughness", *Journal of Physical Oceanography*, vol. 35, no. 5, 835-848
[10] S. Bhattacharya, 2014, "Challenges in Design of Foundations for Offshore Wind Turbines", *Engineering & Technology Reference*, 9-20.
[11] D. J. Tritton, 1988, "Physical fluid dynamics", 2nd ed., Oxford: Clarendon Press.
[12] ANSYS Inc. 2016, ANSYS Fluent User's Guide, Release 17.2
[13] N. V. Nikitin, F. Nicoud, B. Wasistho, K. D. Squires and P. R. Spalart, 2000, "An approach to wall modelling in large-simulations," *Phys. Fluids*, Vol. 12, 1629-1632.
[14] P. R. Spalart, S. Deck, M. L. Shur, K. D. Squires, M. Kh. Strelets and A. Travin, 2006, "A new version of detached-eddy simulation, resistant to ambiguous grid densities," *Theor. Comput. Fluid Dyn.*, Vol. 20, 181-195.
[15] B. Blocken, T. Stathopoulos and J. Carmeliet, 2007, "CFD simulation of the atmospheric boundary layer: wall function problems", *Atmospheric Environment*, vol. 41, no. 2, 238-252.
[16] T. Nishino and S. Draper, 2015, "Local blockage effect for wind turbines", *Journal of Physics: Conference Series*, vol. 625, 012010.